Influence of Holdup on Gas and Particle Flow Patterns in a Spiral Jet Mill

L. Scott, A. Borissova, A. Burns, and M. Ghadiri*
School of Chemical and Process Engineering, University of Leeds, Leeds LS2 9JT, UK

*Contact Email: M.Ghadiri@leeds.ac.uk; *Tel: 0044(0) 113 343 2406

Abstract

Particle size reduction in spiral jet mills is induced by high velocity gas jets, causing interparticle and particle wall collisions leading to breakage. Despite extensive research on the design and operational parameters, the underlying mechanics of size reduction is still poorly understood. Discrete Element Method and Computational Fluid Dynamics are used here to analyse particle and fluid motions. A fast shearing dense particle bed is formed on the wall, with a transition to lean phase towards the centre of the mill. This necessitates four-way coupling of fluid and particle interactions for analysis. It is shown that increasing the depth of the particle bed reduces the fluid phase tangential velocity in the proximity of the classifier, as momentum is exchanged with circulating particles. The energy dissipation through particle collisions occurs mainly along the bed surface and in front of the grinding jet nozzles.

Keywords: Discrete element method, spiral jet mill, holdup, dissipated energy

Nomenclature

Variable	Description	units
c_d	coefficient of drag	-
v	velocity	m/s
r	radius	m
M	mass	kg
t	time	s
ρ	density	kg/m^3
δ	cut size	m
Subscript		
c	classifier	
g	gas	
p	particle	
r	radial component	
t	tangential component	

Introduction

The spiral jet mill is the equipment of choice in many industries that process particulate solids, as it has no moving parts, low maintenance and contamination of the final product during size reduction. The mill is mechanistically simple and particle breakage is the result of interparticle and particle-wall collisions, brought about by an internal vortex formed by a series of gas jets [1]. Breakage and classification occur simultaneously within the same chamber, and a subtle change in the rate of either will alter the fluid flow field and particle dynamics. During operation of the mill, a bed of particles forms along the outer wall of the milling chamber due to centrifugal action induced by the gas jets, which are inclined at an angle with respect to the tangent to the wall. The layers of the bed are sheared at high strain rates across one another, whilst the high-velocity gas jets eject the particles from the shearing bed and subject them to high energy collisions. Therefore, within the mill, particles undergo size reduction by chipping and fragmentation [2].

The effect of grinding conditions in the mill on the size reduction process has been extensively investigated, indicating that the grinding pressure of the air and the material feed rate are the two factors that significantly influence milling performance [1, 3-7]. It has also been shown that the injector pressure of the feed material only affects the grinding rate if the grinding pressure is low [1, 3, 7]. Nair's work [6] shows an optimum nozzle configuration in terms of nozzle diameter and grinding pressure; smaller nozzles using high pressures can produce more extensive breakage at lower input energy, as compared to larger nozzles using lower pressures. Tuunila and Nyström [1] and Katz and Kalman [7] carried out independent investigations of the effect of nozzle angle, which suggest some optimum angle around 45˚. Luczak et al. [8] highlighted that fewer grinding nozzles elongate the jetting regions and improve milling efficiency when comparing configurations of 4, 8 and 12 jet nozzles.

The holdup of material in the mill plays a significant role in the particle dynamics, affecting both the motion of the particles and their interactions. Predicting the motion of interdependent two-phase centrifugal flow field is very challenging, as the particle concentration changes abruptly from a fast moving and shearing dense bed to a lean phase flow. The large number of particles entrained within the gas substantially influence both the gas and particle flow fields [4, 9, 10]. Kürten and Rumpf [11] carried out some of the earliest investigations into flow behaviour in a spiral jet mill, using triboluminescent dyes and water. They report that comminution is prominent along the *Rückseite* (backside) of the jets. However, this did not meet their expectations, as they had postulated that increased grinding should be seen along the *Vorderseite* (frontside) of the jets [12]. Considering the geometry of the spiral jet mill, as shown in Figure 1, and in order to facilitate the description of the jet geometry, the front- and back-sides of a jet are highlighted in Figure 2. The bed circulates clockwise due to the jet angle, and therefore the front of the jet is presented to the oncoming particles. Kozawa et al. [13] similarly used dye in a water-filled mill to show that the flow may shortcut out of the

milling chamber. Müller et al. [4] investigated the holdup and residence time of particles within the milling chamber using a radioactive tracer. They found that the holdup decreased, as the grinding pressure was increased. Rodnianski et al. [9] used a combination of CFD and physical experiments to predict the ratio $\left(\frac{v_{t,p}}{v_{r,p}}\right)$ of a particle that would allow it to be classified. However, they concluded that CFD is only effective at predicting the fluid field with no particle holdup present. MacDonald et al. [10] derived a series of analytical functions consisting of multiple parameters that included particle holdup, to predict a particle cut size that could be removed from the milling chamber. Luczak [14] and Luczak et al. [8] used particle image velocimetry within the milling chamber to analyse the flow patterns for different particle feed rates and grinding pressures. Luczak [14], in contrast to Kürten and Rumpf's [12] findings and in agreement with their original expectation, found that grinding intensity is increased along the frontside of the jet, as the particles are ejected from the bed.

There is a significant radial variation of particle concentration in a spiral jet mill, as particle flow is in a dense rapid shearing bed near the wall and in a lean phase towards the centre due to the centrifugal flow field. For such cases, the most appropriate analysis method is by Coupled Computational Fluid Dynamics – Discrete Element Method (CFD-DEM) modelling. However, despite this approach being over 20 years old [15], its capability is still very limited for fine particles undergoing size reduction due to limitations of computational power and large number of particles [2, 16-18]. This has often led to simplifications to decrease computational time. Teng et al. [19] analysed particle collisions and concluded that inter-particle collisions had a relative velocity that was higher than that of particle-wall collisions. They also reported that during particle collisions, the average tangential component of the contact force was eight times larger than the normal component. This led to the conclusion that particles collided in a "side-swipe" motion and therefore, abrasion was the largest factor driving particle size reduction. However, their findings were based on a very dilute system, which consisted of only

4

1000 particles. Therefore, their findings do not reflect the entire behaviour of the mill. Brosh [20] carried out numerical simulations with his own in-house DEM code, coupled with ANSYS-Fluent, and reported a good agreement with physical experiments describing particle motion in a spiral jet mill. Later, Brosh et al. [21] incorporated breakage using both impact and fatigue breakage functions for size reduction in their simulations. However, the particle stiffness was artificially reduced so that the DEM time-step could be increased, the effect of which on particle breakage requires further evaluation. Particles were also removed from the simulation once their diameter decreased below 10 μm, rather than allowing the particles to be classified. Dogbe et al. [2] carried a thorough parametric study and showed that the smallest particles had the highest collision frequency and were responsible for a large amount of total energy dissipation. More recently, Bnà et al. [18] used a one-way CFD-DEM coupling to predict size classification. They found good agreement with the cut size equation, originally proposed by Dobson and Rothwell [22]:

$$\delta_{cut} = \frac{3}{4} \frac{c_d \rho_g r_c}{\rho_p} \left(\frac{(v_{r,g})^2}{(v_{t,g})^2} \right)$$
Eq. 1

where c_d is the particle drag coefficient, r_c is the classifier radius, $v_{r,g}$ is the radial component of the gas velocity, $v_{t,g}$ is the tangential component of the gas velocity, and ρ_g and ρ_p are the gas and particle densities, respectively. However, Bnà et al. [18] indicate that one-way coupling is satisfactory only when the mill is operated as a classifier. The instantaneous particle loading dampens the fluid field and alters the local fluid velocity, necessitating the use of four way coupling for fluid and particle interactions.

As the holdup plays a crucial role in size reduction, a range of different mass loadings in a spiral jet mill are simulated, using the four-way coupling of CFD-DEM approach [15, 23-25]. Inter-particle and particle-wall collisions are analysed as a function of holdup, as influenced by the fluid flow field. Breakage and classification are not addressed in this study, as the focus is

on the influence of holdup and associated dynamics of the moving bed under the centrifugal field on both particle and fluid flow field patterns and collisional energy dissipation.

Method

The mill used in the simulations is based on the design of the Hosokawa Micron AS-50 spiral jet mill. The main chamber has a diameter of 50 mm, with four angled jets with respect to the tangent that are equally spaced around the outer wall. Important design features are shown in Figure 1, which includes both an in-house CAD drawing, based on measured physical dimensions, and the geometry used in the simulations. The design of the mill is such that the gas flow in the central region is constricted, making it first spiralling upwards into a hemispherical chamber and then changing direction and spiralling downward and out of the mill. The manifold section that supplies high pressure air to the four jet nozzles is also included, as Dogbe [26] has shown this feature being important in influencing the flow field. The feed particle injector nozzle and the associated funnel are also included, as Dogbe [26] has shown that the induced air flow through the funnel has a considerable affect on the fluid flow field in the grinding chamber. The top view of the funnel can be seen as a circle on the right drawing of Figure 1 at 7 o'clock position. However in these simulations, particles are not introduced via the funnel, but placed directly within the chamber to save simulation time. Nevertheless the injector nozzle supplies the presurrised air as in real experiments, causing the induced air to be sucked into the chamber. The injector nozzle and the eductor cone, entraining the surrounding air can also be seen in Figure 1, entering the chamber at an inclined angle (shown on the left drawing) and at a mid-radial position (shown on the right drawing). For each mass loading investigated, the rate of material addition into the chamber is altered so that all particles are added within 0.01 s time.

Figure 1: An in-house made CAD drawing of Hosokawa Micron AS-50 mill (left). Simulation geometry in EDEM™ with particle generation zone as a disk is highlighted in red (right).

The particles are taken as spheres and their motion is calculated using EDEM 2019 (DEM Solutions, UK), and the fluid flow field is resolved by ANSYS Fluent 18.1. As mentioned above, a four-way coupling scheme is adopted in this work to capture all particle-fluid interactions. The drag model by Morsi and Alexander [27] and the k-ε-RNG turbulence model with scalable wall functions are implemented in Fluent 18.1. A tetrahedral mesh pattern is employed for CFD. The mesh size is based on the largest particle size (300 μm), from which a maximum volume of 40% particle-to-fluid cell ratio is chosen, as recommended by Norouzi et al. [28]. The particle contact model used in EDEM 2019 is the Hertz-Mindlin model [29, 30]. The time step chosen for the integration is 25% of the Rayleigh time step. The fluid time step used is between 30 and 50 times the particle time step, as recommended by Norouzi et al. [28]. The five mass loadings, the corresponding number of spheres and their size distribution on the mass basis are listed in Table 1. The gas and particle properties used throughout each simulation are given in Table 2. The friction and restitution coefficient are typical and commonly used values for DEM simulations. Before particles are added into the milling chamber, the fluid field is allowed time to resolve. A pressure of 3 barg has been selected for the grinding pressure. The pressure is low under normal operating conditions, however, it was chosen as it has been used extensively in previous works [2, 26]. The injector pressure nozzle was set to 3.2 barg.

Table 1: Holdup mass loadings and particle size distribution used in the simulations

Table 2: Fluid and particle properties and associated simulation conditions

Fluid field

Velocity magnitude contour plots of the fluid field for each holdup loading are shown in Figure 2, where the velocity scale ranges from 0 to 100 m/s. The air velocity entering the chamber is around 300 m/s. However, the velocity range presented here has been limited to 100 m/s so that the low velocities are made more visible. There are three distinct regions within the grinding chamber; one occupied by the particle bed, another forming the lean phase between the bed and centre, and the third one being the region of the fast swirling fluid field close to the central classifier. The slowest velocity is denoted by blue colour; around 0 to 10 m/s, whereas the higher velocities are coloured green and then red; 50 m/s and 100+ m/s, respectively.

At the wall of the chamber, the darkest blue region represents the depth of the moving particle bed. The high dampening of the air flow caused by the bed of particles leads to a much lower fluid velocity within this section of the milling chamber. The light blue colour represents dispersed particles present above the moving bed. Moving further towards the centre of the chamber, in the region of the mill highlighted in green, there is such an insignificant number of particles present that the forced vortex is unaffected by dampening. Finally, around the classifier, a free vortex is formed which spirals upwards due to the classifier geometry (i.e. the lip on the base and the cap on the chamber ceiling, cf. the right drawing of Figure 1). The air then changes direction, aided by a conical vortex finder at the top and spirals downward out of the central port. This final increase in velocity is represented by yellow and red regions at the centre of each image in the figure. Compared to the experimental velocity profiles reported by

8

Luczak [14] and Luczak et al. [8], based on particle velocimetery, there is good qualitative agreement for the flow field with their results, despite differences in the mill size and and nozzle numbers.

Clearly observed in the 2.0 g case (Figure 3), there is a distinct transition in the fluid flow patterns between the bed and the lean phase regions of the mill. As particles reside mainly within the moving particle bed, indicated by the large dark blue region, the jet penetration depth is short in this case and limited to the bed depth, and the fluid velocity is dampened. In contrast, in the 0.4 g case, the jets extend far outside the bed depth, with the 1.2 g case lying somewhere in between the extremes.

As the jet penetration length decreases with increasing particle loading, so too does the gas velocity surrounding the classifier. In the 0.4 g case, the magnitude of the gas velocity around the classifier approaches 100 m/s, whereas, in the 2.0 g case, it does not exceed 80 m/s and the region occupied is much smaller. However, there is no direct dampening of the air surrounding the classifier by the particles, as they do not orbit so closely to classifier ring. Instead, the decrease in velocity around the classifier is a result of momentum transfer with the particles within the bed and reduction in air flowing radially towards the centre of the mill, as the jets become less able to penetrate through the particle bed.

Figure 2: Velocity magnitude of the fluid field for different holdup loadings after the particles have been added and the kinetic energy has stabilised (top view)

This is further observed by plotting the radial and tangential velocity components of the air separately. In Figure 3 (a) and (c), the radial velocity component of the gas phase is shown for

the 0.4 g and 2.0 g cases, respectively. The velocity in both images has been limited to -70 to 30 m/s for better visualisation of the fluid field in the central region of the chamber. The radial velocity in the lean phase region of the mill for the 2.0 g solids loading case is positive (outward) and large (around 15-25 m/s) behind the jets, indicating air entrainment into the jets. Elsewhere the radial velocity is largely zero, except at the nose of the jets, where it is along the jet direction. In comparison, the lean phase region for the 0.4 g case, has largely a negative radial velocity (inward) around -5 m/s, indicating a forced vortex there, except a small region behind the jet at the 3 o'clock position, and to a much lesser extent for the jet at the 9 o'clock position. Interestingly, the fluid flow field is not fully symmetric, due to the position of the injector nozzle (cf. Figure 1). Images (b) & (d) in Figure 3 present the gas tangential velocity component for the 0.4 g and 2.0 g solids loading cases, respectively. Again, the velocity has been limited to between -120 m/s and 20 m/s to intensify and highlight the fluid flow field in the central region. The tangential velocity component is much larger than the radial one, and therefore it has a greater effect on the overall fluid flow profile. This is the reason why images (b) and (d) are similar to images in Figure 2. However, in Figure 3 the images show that the tangential component decreases as the holdup loading is increased. It is notworthy that the entrained air throught the funnel, having a mass flowrate as calculated by Dogbe [26] is likely to decrease with an increase in the holdup, thereby decreasing tangential momentum of both the fluid and the particles.

Overall, the fluid phase ability to drag the particles radially towards the centre increases as the holdup loading is increased, whilst the tangential momentum of the particles diminishes. It follows then that the ratio of tangential velocity to radial velocity decreases and therefore the theoretical cut-size presented in Eq. 1 should increase. However, the particles used in this study are larger than this cut-size and therefore this finding could not be substantiated.

Figure 3: Images (a) and (b) depict the air radial and tangential velocity profile for 0.4 g case, respectively. Image (c) and (d) depict the air radial and tangential velocity profile for 2.0 g case, respectively.

Particle Phase results

The particle velocity magnitude as a function of the radial position from the chamber wall is shown in Figure 4. A moving average with an interval consisting of 30 measurements is used in the radial direction to show the local mean particle velocity. The data are collected from a slice having a thickness of $8d_p$ and height of the milling chamber and at circumferential position 45° from the gas nozzle N1 shown in Figure 5. Each plot therefore presents the data in a segment of the slice and has been limited to a distance 12 mm from the chamber wall, as few particles travel further radially. The data from 200 time intervals are used.

The 0.4 g case has the highest average velocity for all five cases, as fewer particles are accelerated as compared to higher loadings, due to longer mean free path and more fluid available per unit mass. Moreover, the dense bed is shallower. The velocity at the wall is around 3 m/s and increases until the particles are at a distance of 7.5 mm, after which it begins to decrease. For this case, the bed is actually only around 1 mm in thickness, yet there is a velocity gradient indicating the different shearing layers of particles. The 0.8 g and 1.2 g cases show a similar trend, though the overall distribution is lower than the 0.4 g case, indicating a reduction in the average velocity for the entire particle system.

Interestingly, the trend slightly alters in the 1.8 g and 2.0 g cases. The increase in bed size has dramatically decreased the particle velocity, as the initial section of each plot appears shallower than the other cases and flat. The particles are still moving at the bed wall, yet their behaviour with neighbouring layers could be considered as 'plug-flow'. This indicates a lack of shearing at the bed wall for the higher loading cases.

11

Figure 4: Profile of particle velocity magnitude as a function of distance from the outer wall for different holdup loadings.

Figure 6 presents the velocity magnitude for each mass loading and is constructed using the same method as in Figure 4, i.e. plotting the average particle velocity at the corresponding radial position. For consistency, each image is plotted from 0 to 30 m/s and colour-coded using the default colour-map of FLUENT. In each image, there is a dark blue ring around the wall the milling chamber, representing the particle bed, wherein the particles travel at the lowest velocities found in the chamber. The particles travelling at the highest velocity can be seen in the dark red regions, along the jet length. There is also a region at the base of the jet where there is particle pileup in the dense circulating bed due to the jet angle.

As the mass loading is increased, the depth of the particle bed increases, accordingly, shown as the blue ring images (a) - (e). The air jets eject the particles out of the bed, as a result of which the bed depth become shallow immediately aft the jet base. However, it gradually recovers until it impinges onto the following jet.

The development of a dense bed structure advocates the use of full four-way coupling CFD-DEM to account for interparticle-fluid interactions. Bnà et al. [18] found that particle-wall collisions occurred with a much higher velocity than particle-particle collisions. They recorded particle-wall collisions higher than 110 m/s. However, Figure 4 and 6 do not corroborate their findings once the particle bed has been established. Particles move much slower along the wall, and therefore, are exposed to lower collision velocities. However, one-way coupling cannot model the influence of particles on the fluid flow field, and hence the local gas velocity remains unchanged.

In order to depict the distribution of the particle population density in the mill and their velocity, data are collected from three slices as shown in Figure 5. The slices are positioned at 0°, 30°, 60° from a jet. They have the same height as of the mill and a width of $8d_p$ to enable capturing a sufficient number of particles at a single set time. The centre position of each particle within each slice is shown as a dot, which is colour-coded to indicate its velocity. The data for each slice are presented on a two dimentional plane, encompassing the axis and radius (r-z plane) in Figure 7. For brevity, only the holdup loadings of 0.4 g and 1.6 g are presented. As in Figure 4 the particles with a radial distance greater than 12 mm from the wall are not illustrated in order to improve visualisation of the particles closer to the wall. In the 0.4 g case, there is little variations between images (a), (c), and (e). The particle bed has recovered its shape in image (c), so the disturbance caused by the jet cannot be seen.

Figure 6: Contour plot of particle velocity (top view on z-plane), as holdup loading is increased. Images (a), (b), (c), (d) and (e) represent the cases 0.4 g, 0.8 g, 1.2 g, 1.6 g and 2.0 g, respectively.

In Figure 7, however, the influence of the high pressure jets on particle flow field can be seen more clearly in the 1.6 g case. Overall the particles occupy the bed volume uniformly along the z direction at the N1 jet position, i.e. 0°, similar to the 0.4 g case. This is with the exception of the area directly in front of the nozzle at mid-height position (i.e. the base of the jet), where the particle concentration is lower than elsewhere, referring to image (b). The particle velocity gradient can be inferred from the colour coding of the dots. There is some minor crowding of

the particles on the ceiling and base of the chamber. The angled base of the mill is also visible in the image and is the reason for the particle bed base sloping downwards. Past the jet position and particles ejected from the bed as shown in image (d), the bed surface appears undulated, inferred from tracing dots of a single colour along the height. The particle loss from the bed reduces its depth near the ceiling and base of the chamber. The bump around the mid-height position is due to the angled action of the jet, conveying the particles to this region. Particles ejected by the jet (as shown by red dots) can be distinguished easily, as they have a high velocity, greater than 20 m/s and are farthest from the wall. In image (f), the majority of particle that had been ejected from the bed have now returned, as the bed depth has not only recovered, but in fact has become even deeper than that of the bed in image (b). Clearly at high holdup loadings, interparticle collisions are dominant as compared to particle wall, and the jet action shears the paricles out of the bed and makes them collide with the bed surface farther downstream. It is noteworthy that the dense bed moves more as a plug near the wall, particularly for deeper beds. This is also shown in Figure 4, where for 1.6 g and 2.0 g cases the velocity is relatively flat near the wall. This implies that fast shearing near the bed surface and the radial velocity component of the entrained particles in the jets, as shown in Figures 6 and 7, are responsible for the milling process.

Figure 7: Scatter graphs of particle position and velocity (colour-coded) for 0.4 g (left) and 1.6 g holdup loadings (right). Each image corresponds to the slice shown in Figure 6, starting with the leftmost jet first, i.e. N1: Images a and b for 0°, c and d for 30°, and e and f for 60 °.

The temporal evolution of total kinetic energy ($E = \sum_{i=1}^{n} M_i v_i^2$) of the particles accumulated over the time t=0 to t=0.06 s is shown in Figure 8. Particles are added to the mill at different

rates to ensure that all particle feeding is complete within 0.01 s for all cases; e.g. the feed rate for the 2.0 g case was 0.2 kg/s. The initial velocity of each particle is set to zero. It can be seen in each image that there is a steep increase in the system kinetic energy, as the initial small number of particles are accelerated quickly in the chamber. The total kinetic energy of the system then continues to increase in each case. There is a peak that develops at about 0.01 s, which is most visible for the higher loading cases, for which the addition rate is higher. This is presumably due to initial unsteady motion of the bed. The same is also true of the other minor variations in the system kinetic energy between each of the five cases. The system can be regarded as operating at steady-state after time t = 0.03 s, as the kinetic energy for each of the five cases appears to have stabilised. This is consistent with the work of Dogbe et al. [2], where similar simulations were carried out. It was found that 0.03 s was a sufficient length of time for the particles to disperse and reach steady-state.

Figure 8: **Temporal variations of the total particle kinetic energy accumulated from time t = 0 s to 0.06 s**

Using the data shown in Figure 8 from t = 0.03 s to 0.06 s, the average kinetic energy of the system is calculated. For each holdup loading, the average kinetic energy of the system reaches an asymptotic value of approximately 7 J. Surprisingly, despite the increase in mass loading, there is little variation in the total kinetic energy between the cases. The underlying reason is unclear, but this is presumably due to the total fluid power being the same in all cases. However, as the mass loading is increased, there is a 15% increase in the energy dissipation rate from 4.05 W to 4.65 W. Therefore, the particle system is actually dissipating more energy as the mass loading is increased.

Another reason for the decrease in the fluid flow field velocity is the presence of the particles altering the turbulent properties of the fluid phase. The presence of particles in the fluid field should attenuate turbulence, locally however, the particles may increase the shear rate of the fluid, or increase the turbulent production term through wakes [31]. When in large clusters, such as a bed, they will alter the flow pattern of the fluid, and may also affect the finite fluid volume cell when significantly loaded [32, 33]. Comparing the turbulent kinetic energy term for the two cases of 0.4 g and 2.0 g, it can be observed in Figure 9 that the production of turbulent energy has indeed increased with particle loading. Luczak [14] also observed a distinct increase in the turbulent kinetic energy in the lean phase region of the mill as part of their particle image velocimetry study.

Figure 9: Turbulent kinetic energy (J/kg) plot of the fluid flow field for 0.4 g and 2.0 g holdup loadings after t = 0.06 s.

The spatial distributions of collision energy and frequency are shown in Figure 10. The contour plots are constructed in the same manner as Figure 4 and the data are collected from t = 0.03s to 0.06 s. Images (i), (ii) and (iii) depict the collision frequency for the 0.4 g, 1.2 g and 2.0 g cases, respectively. Areas of high collision frequency are coloured red, scaling through orange, yellow, green, and finally blue, which denotes areas where few collisions are recorded. In image (i), high collision frequency is recorded next the chamber wall only and increases further before each jet. The small amount of material creates a shallow particle bed, and shearing layers pass over one another in close proximity to the wall. There is also a minor particle pile-up

before the nozzles that increases the collision frequency further, as particles in the jet regions are accelerated out of the bed. Particles outside the bed travel with similar direction and magnitude, and therefore collide infrequently. This results in the large area of dark blue observable in the image. In image (ii), the particle bed has become deeper and the largest areas of collision frequency is at the bed surface and along the frontside of the jets, as shown by the red colour in the image. As discussed previously, the particles at the bed surface travel at a higher velocity, compared to those particles closer to the wall. As a result, the particles at the bed suface are brought into contact more frequently, as the layers shear across one another. The large number of particles returning to the bed after being expelled by the jets (not visible in this image), further increases the number of collisions recorded at the bed surface. Pile-up before the jets has also become more prominent, compared to the 0.4 g case. As a result, the particles now begin to build-up and shear along the frontside of each jet. The same and more noticeable behaviour is also viewed in image (iii). However, the colour gradient has greater prominence in the particle bed, owing to the greater disparity in particle velocity across thebed depth.

Images (iv), (v), (vi) depict the dissipated energy distribution of the largest recorded value for a single collision in the mill for the three cases. The dissipated energy is calculated from the change in velocity due to collision. Once again, a colour scheme of blue to red is used to depict the energy values from low to high, respectively. In all the cases, the largest values of dissipated energy are in front of the jets, as well as in the regions where the particles are being sheared, as shown by the red colour. For the large holdup loadings the areas of high dissipated energy are mainly at the bed surface and in the positions in front of each jet. Comparing the 2.0 g case with the 0.4 g and 1.2 g cases, it can be seen that there are few high energy collision. This can be attributed to the decrease in velocity, as shown in Figure 4, as well as to the increase the increase in collision frequency.

Finally, images (vii), (viii) and (ix) depict the cumulative dissipated energy over the 0.03 s of simulation time. In the 0.4 g case, the combination of high collision frequency and particles re-entering the bed with a greater than average velocity results in areas of the mill associated with high energy dissipation. However, at this mass loading the milling chamber is underfilled, and the particle bed has not fully formed. Instead, the 1.2 g and the 2.0 g cases depict the cumulative dissipated energy more realistically. In the images (viii) and (ix), it can be clearly seen that the energy dissipation occurs mostly along the bed surface and directly in front of the jet nozzles. At the bed surface, particles are sheared at the highest rate and are exposed to high velocity collisions with other particles re-entering the bed after being ejected. In front of the jets, particles are suddenly accelerated at an inclined direction with respect to the tangent to the wall. The result is a collision with greater relative velocity, and therefore, more energy is dissipated during the contact. This is in agreement with the work of Luczak [14], who found that comminution is prevalent along the frontside of the jet, but in contrast to the findings of Kürten and Rumpf [12], who showed grinding to be prevalent along the backside of the mill.

Once particles are ejected into the lean region, collisions now occur at a higher velocity, but with a much lower relative velocity. Consequentially, the total dissipated energy in the lean region decreases. It can also be seen that within the particle bed, the overall energy dissipation is low when compared to the energy dissipated at the free surface. This is also the case for the lean region, where the relative velocity of associated collisions is low, as the particles travel in the same direction. The high particle concentration in the moving bed also inhibits their acceleration, as the particles are constantly subjected to collisions within the shearing layers. Lastly, comparing images (viii) and (ix), it can viewed that the overall intensity of cumulative dissipated energy decreases as mass loading is increased, in agreement with Katz and Kalman [7].

Figure 10: Contour plots depicting the spatial distribution of collision frequency and dissipated energy within the milling chamber for the 0.4 g, 1.2 g and 2.0g, from t = 0.03 s till 0.06 s.

Conclusions

The dynamics of particle and fluid motion in a spiral jet mill (The AS-50 spiral jet mill of Hosokawa Micron) was simulated using a 4-way coupled CFD-DEM approach to analyse the role of holdup within the main milling chamber. Four holdup mass loadings were simulated. It is shown that as mass loading is increased, the gas velocity magnitude surrounding the classifier zone of the spiral jet mill decreases. The energy lost through momentum transfer to the particles lowers the gas velocity directly surrounding the classifier section of the chamber. Decomposing the fluid flow field shows that as the mass loading is increased, the tangential component of the gas velocity decreases, whilst the radial component increases in magnitude. This should increase the cut-size given the change in the velocity components of the fluid flow field.

Increasing the number of particles in the mill decreases the average velocity of individual particles and leads to less energetic collisions. However, at the same time, the frequency of collisions increases, and therefore, the total energy dissipated from all collisions remains almost constant.

The kinetic energy of the particle system does not vary greatly with the mass loading. It is thought that because of the fluid power does not change, there is no means by which the total kinetic energy of the particle system may alter.

Finally, the distribution of the dissipated energy in the mill chamber indicates that the highest dissipated energy is at the bed surface. A combination of increased shearing and particle

impacting on the bed surface leads to high energy transfer and dissipation. There is also high energy dissipation in front of each jet, where particles are accelerated with a change in the direction. This increases their relative collision velocity and increases the dissipated energy.

Acknowledgements

References

[1] R. Tuunila and L. Nyström, "Technical note effects of grinding parameters on product fineness in mill grinding," *Minerals Engineering,* vol. 11, pp. 1089-1094, 1998.

[2] S. Dogbe, M. Ghadiri, A. Hassanpour, C. Hare, D. Wilson, R. Storey*, et al.*, "Fluid-particle energy transfer in spiral jet milling," *EPJ Web of Conferences,* vol. 140, 2017.

[3] M. Ramanujam and D. Venkateswarlu, "Studies in Fluid Energy Grinding " *Powder Technology,* vol. 3, pp. 92-101, 1969.

[4] F. Müller, R. Polke, and G. Schädel, "Spiral jet mills: hold up and scale up," *Int. J. Miner. Process.,* vol. 44-45, pp. 315-326, 1996.

[5] S. Palaniandy, K. A. M. Azizli, H. Hussin, and S. F. S. Hashim, "Effect of operational parameters on the breakage mechanism of silica in a jet mill," *Minerals Engineering,* vol. 21, pp. 380-388, 2008.

[6] P. Nair, "Breakage parameters and the operating variables of a circular fluid energy mill Part II. Breakage rate parameter," *Powder Technology,* vol. 106, pp. 54-61, 1999.

[7] A. Katz and H. Kalman, "Preliminary Experimental Analysis of a Spiral Jet Mill Performance," *Particle & Particle Systems Characterization,* vol. 24, pp. 332-338, 2007.

[8] B. Luczak, R. Müller, C. Kessel, M. Ulbricht, and H. J. Schultz, "Visualization of flow conditions inside spiral jet mills with different nozzle numbers– Analysis of unloaded and loaded mills and correlation with grinding performance," *Powder Technology,* vol. 342, pp. 108-117, 2019.

[9] V. Rodnianski, N. Krakauer, K. Darwesh, A. Levy, H. Kalman, I. Peyron*, et al.*, "Aerodynamic classification in a spiral jet mill," *Powder Technology,* vol. 243, pp. 110-119, 2013.

[10] R. MacDonald, D. Rowe, E. Martin, and L. Gorringe, "The spiral jet mill cut size

equation," *Powder Technology,* vol. 299, pp. 26-40, 2016.

[11] H. Kürten and H. Rumpf, "Zerkleinerungsuntersuchungen mit triboluchmineszierenden Stoffen," *Chemie Ingenieur Technik,* vol. 38, pp. 331-342, 1996.

[12] H. Kürten and H. Rumpf, "Strömungsverlauf und Zerkleinerungsbedingungen in der Spiralstrahlmuhle," *Chemie Ingenieur Technik,* vol. 38, pp. 1187-1192, 1966.

[13] K. Kozawa, T. Seto, and Y. Otani, "Development of a spiral-flow jet mill with improved classification performance," *Advanced Powder Technology,* vol. 23, pp. 601-606, 2012.

[14] B. Luczak, "Flow conditions inside spiral jet mills and impact on grinding performance," PhD Thesis, Universitat Duisburg-Essen, Essen, 2018.

[15] Y. Tsuji, T. Tanaka, and T. Ishida, "Lagrangian numerical simulation of plug flow of cohesionless particle> in a horizontal pipe " *Powder Technology,* vol. 71, pp. 239-250, 1992.

[16] W. Zhong, A. Yu, X. Liu, Z. Tong, and H. Zhang, "DEM/CFD-DEM Modelling of Non-spherical Particulate Systems: Theoretical Developments and Applications," *Powder Technology,* vol. 302, pp. 108-152, 2016.

[17] M. Sakai, "How Should the Discrete Element Method Be Applied in Industrial Systems?: A Review," *KONA Powder and Particle Journal,* vol. 33, pp. 169-178, 2016.

[18] S. Bnà, R. Ponzini, M. Cestari, C. Cavazzoni, C. Cottini, and A. Benassi, "Investigation of particle dynamics and classification mechanism in a spiral jet mill through computational fluid dynamics and discrete element methods," *Powder Technology,* vol. 364, pp. 746-773, 2020.

[19] S. Teng, P. Wang, Q. Zhang, and C. Gogos, "Analysis of Fluid Energy Mill by gas-solid two-phase flow simulation," *Powder Technology,* vol. 208, pp. 684-693, 2011.

[20] T. Brosh, Y. Batat, H. Kalman, A. Levy, and A. B. Brown, "Particle Motion and Classification in a Jet Mill," *Bulk Solids & Powder, Science & Technology,* vol. 3, pp. 83-88, 2008.

[21] T. Brosh, H. Kalman, A. Levy, I. Peyron, and F. Ricard, "DEM–CFD simulation of particle comminution in jet-mill," *Powder Technology,* vol. 257, pp. 104-112, 2014.

[22] B. Dobson and E. Rothwell, "Particle Size Reduction in a Fluid Energy Mill," *Powder Technology,* vol. 3, pp. 213-217, 1969.

[23] B. Vreman, B. J. Geurts, N. G. Deen, J. A. M. Kuipers, and J. G. M. Kuerten, "Two- and Four-Way Coupled Euler–Lagrangian Large-Eddy Simulation of Turbulent Particle-Laden Channel Flow," *Flow, Turbulence and Combustion,* vol. 82, pp. 47-71, 2008.

[24] A. Di Renzo, F. P. Di Maio, R. Girimonte, and B. Formisani, "DEM simulation of the mixing equilibrium in fluidized beds of two solids differing in density," *Powder Technology,* vol. 184, pp. 214-223, 2008.

[25] S. Elghobashi, "Particle-laden turbulent flows: direct simulation and closure models " *Applied Scientific Research* vol. 48, pp. 301-314, 1991.

[26] S. Dogbe, "Predictive Milling of Active Pharmaceutical Ingredients and Excipients " PhD thesis, School of Chemical and Process Engineering, The University of Leeds, Leeds, UK, 2016.

[27] S. A. Morsi and A. J. Alexander, "An investigation of particle trajectories in two-phase flow systems," *Journal of Fluid Mechanics,* vol. 55, p. 193, 2006.

[28] H. R. Norouzi, R. Zarghami, R. Sotudeh-Gharebagh, and N. Mostoufi, *Coupled CFD-DEM Modeling.* Chichester, UK: John Wiley & Sons, Ltd, 2016.

[29] C. Thornton, *Granular Dynamics, Contact Mechanics and Particle System Simulations.* Springer International Publishing Switzerland: Springer International Publishing, 2015.

[30] A. Di Renzo and F. P. Di Maio, "Comparison of contact-force models for the simulation of collisions in DEM-based granular flow codes," *Chemical Engineering Science,* vol. 59, pp. 525-541, 2004.

[31] Z. Yuan and Michaelides, "Turbulence modulation in particulate flows - A theoretical approach," *int. J. Multiphase Flow,* vol. 18, pp. 779-785, 1992.

[32] Crowe, "On models for turbulence modulation in fluid particle flows," *int. J. Multiphase Flow,* vol. 26, pp. 719-727, 2000.

[33] Y. Zhang and J. Reese, "Gas Turbulence Modulation in a Two-Fluid Model for Gas–Solid Flows," *AIChE Journal,* vol. 49, pp. 3048-3065, 2003.
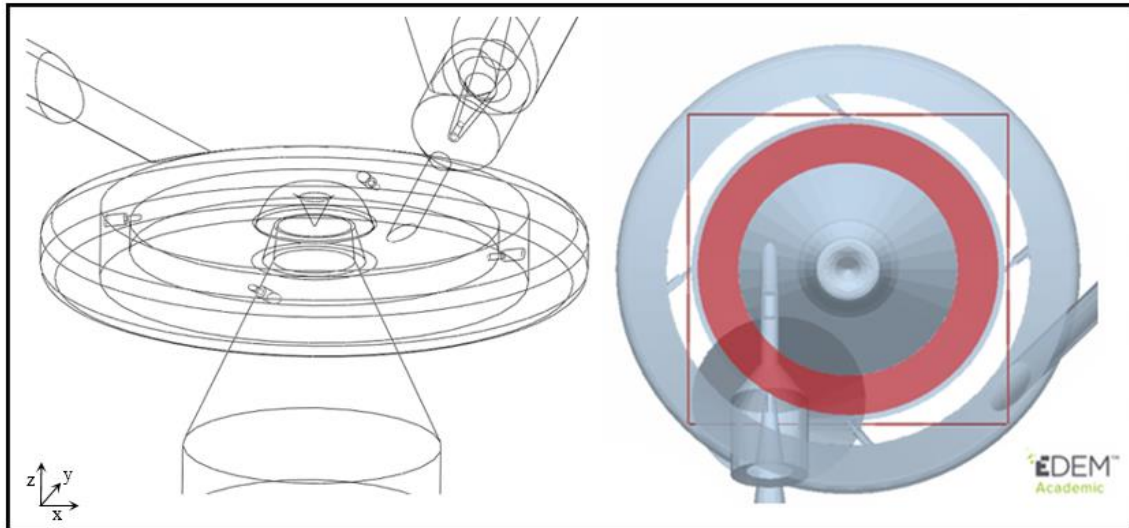
Figure 11: An in-house made CAD drawing of Hosokawa Micron AS-50 mill (left). Simulation geometry in EDEM^{TM} with particle generation zone as a disk is highlighted in red (right).
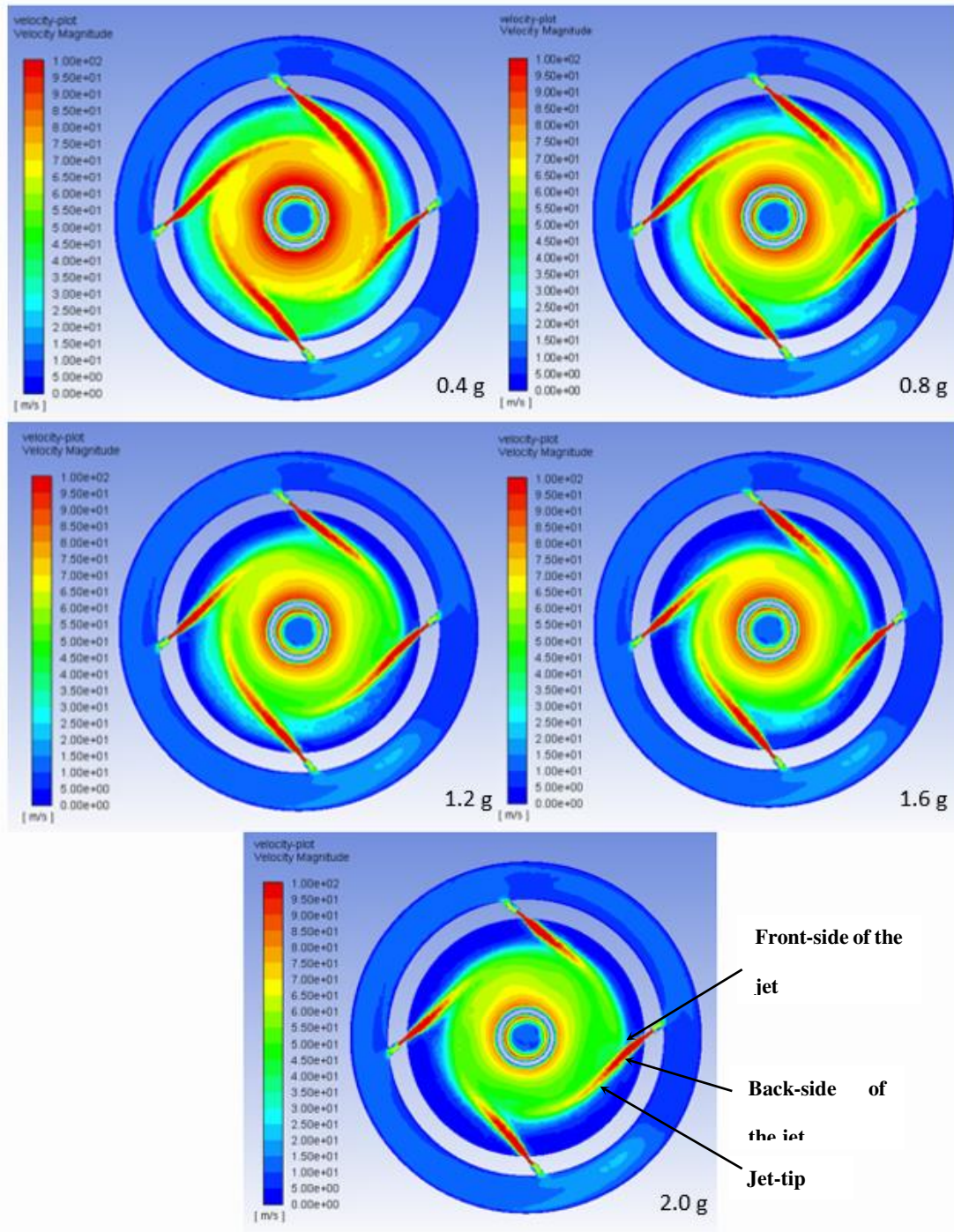
Figure 12: Velocity magnitude of the fluid field for different holdup loadings after the particles have been added and the kinetic energy has stabilised (top view).
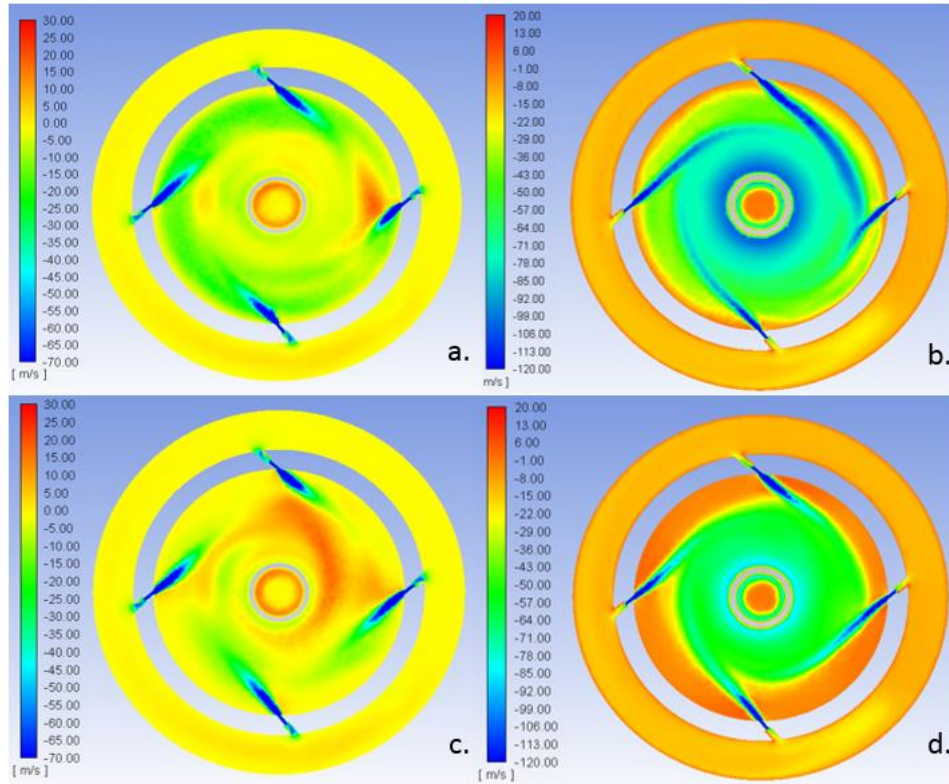
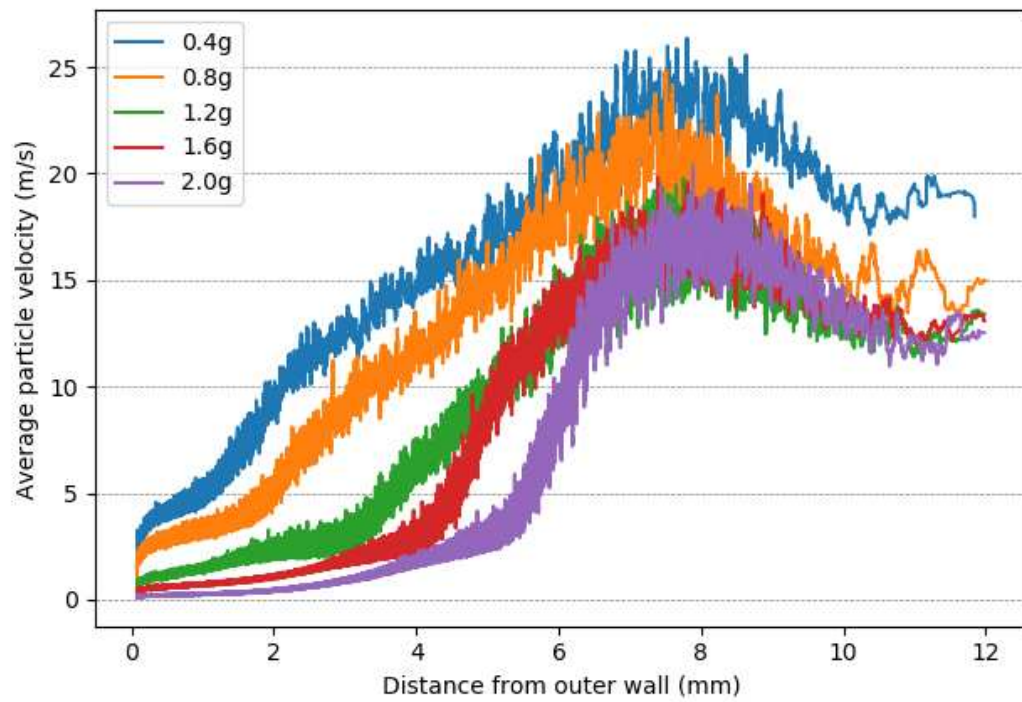**Figure 13: Top view images of the radial (a and c) and tangential (b and d) air velocity profiles for 0.4 g and 2.0 g holdup loadings, respectively.**

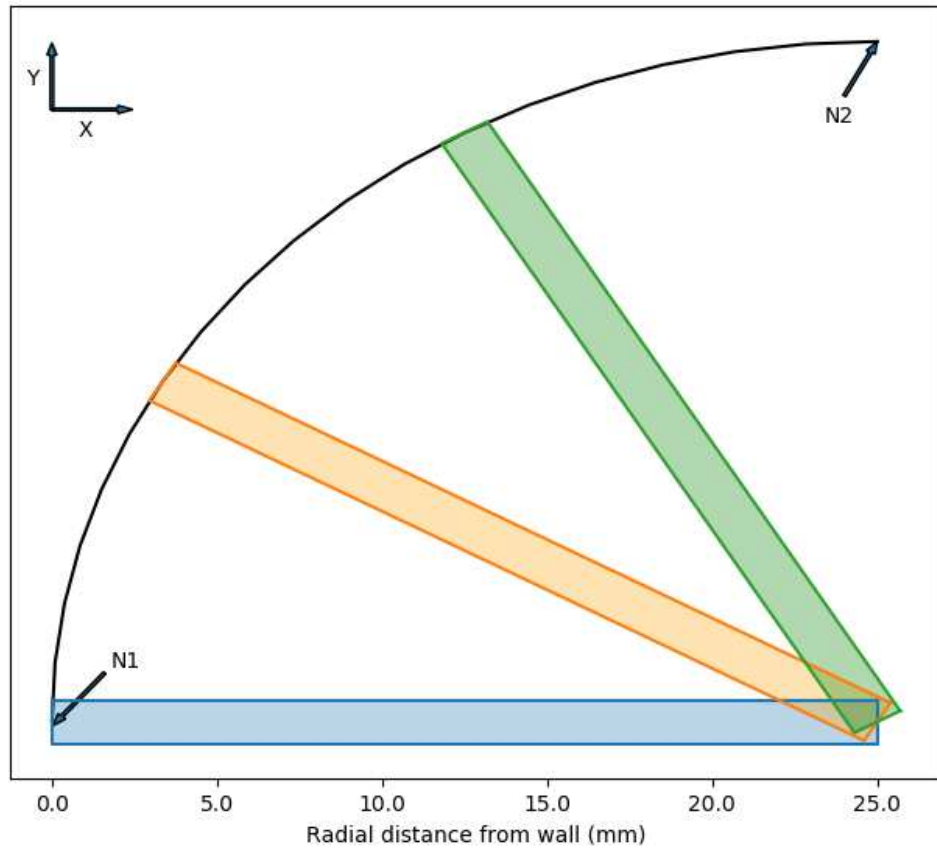**Figure 14: Profile of particle velocity magnitude as a function of distance from the outer wall for different holdup loadings.**

Figure 15: Construction slices used to produce axial plots between two jets. Slices taken at 0° (blue), 30° (orange), 60° (green) from nozzle (N1), having a thickness of 8 average particle diameters.
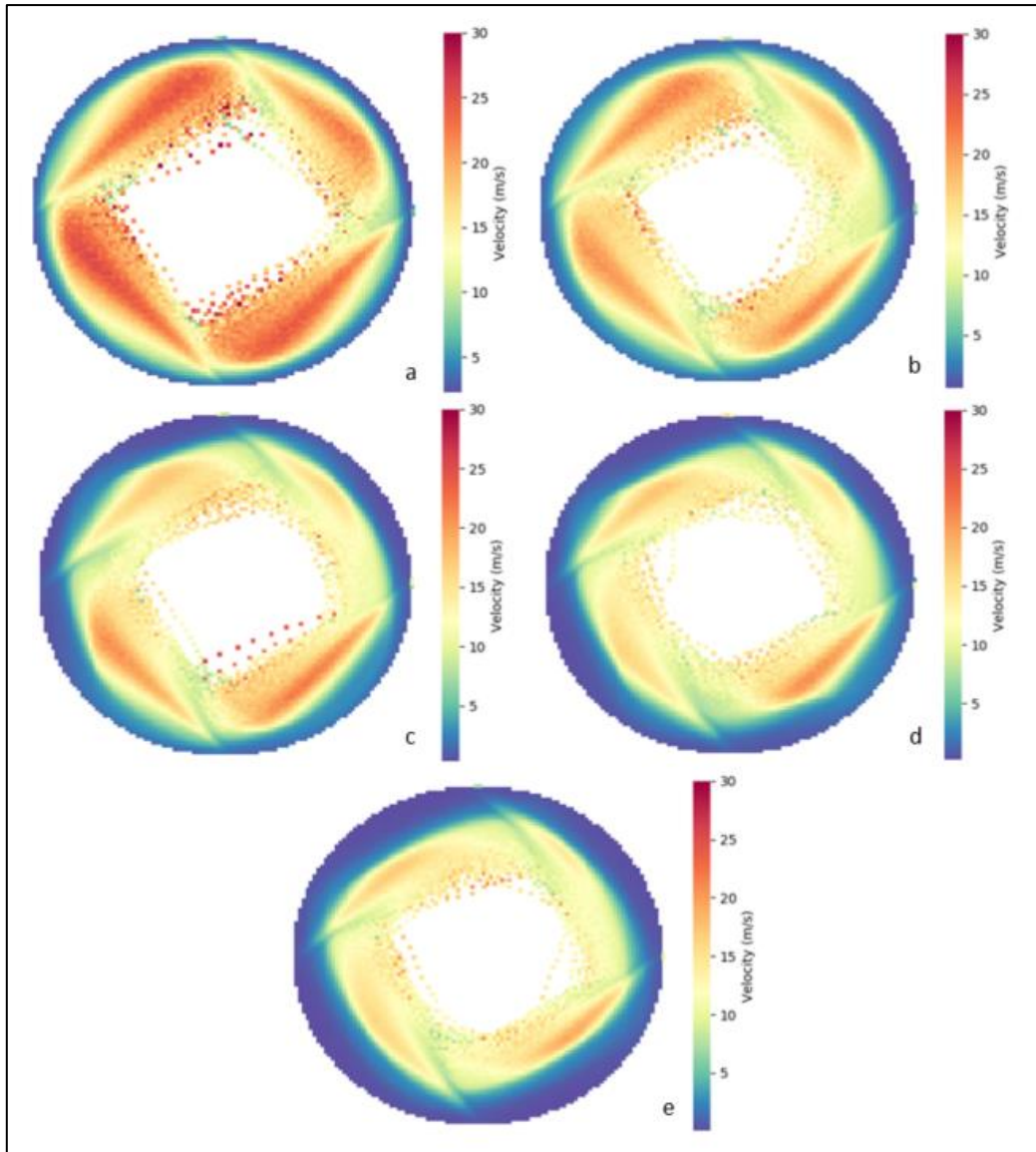
Figure 16: Contour plot of particle velocity (top view on z-plane), as holdup loading is increased. Images (a), (b), (c), (d) and (e) represent the cases 0.4 g, 0.8 g, 1.2 g, 1.6 g and 2.0 g, respectively.
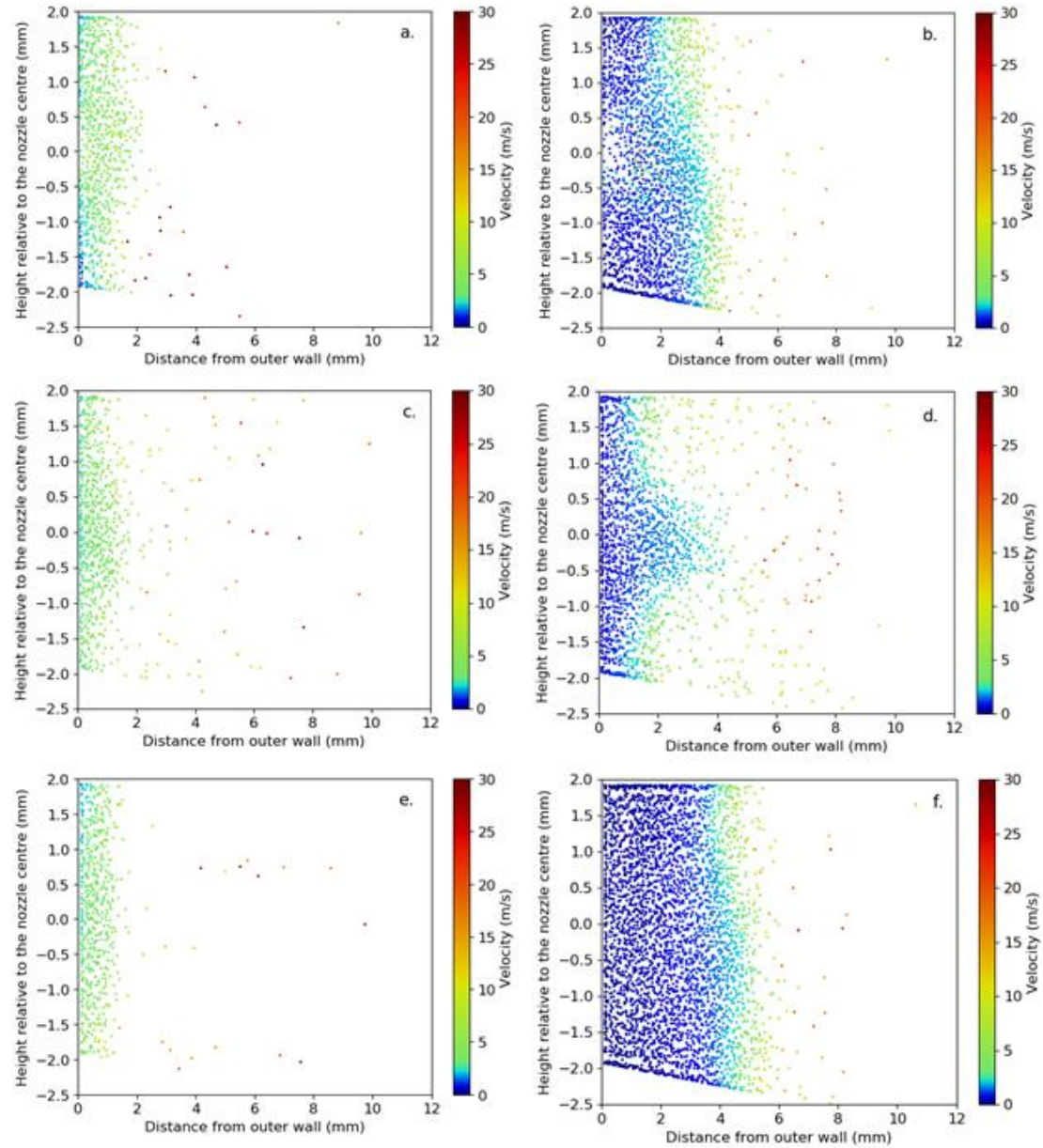
Figure 17: Scatter graphs of particle position and velocity (colour-coded) for 0.4 g (left) and 1.6 g holdup loadings (right). Each image corresponds to the slice shown in Figure 5, starting with the leftmost jet first, i.e. N1: Images a and b for 0°, c and d for 30°, and e and f for 60 °.
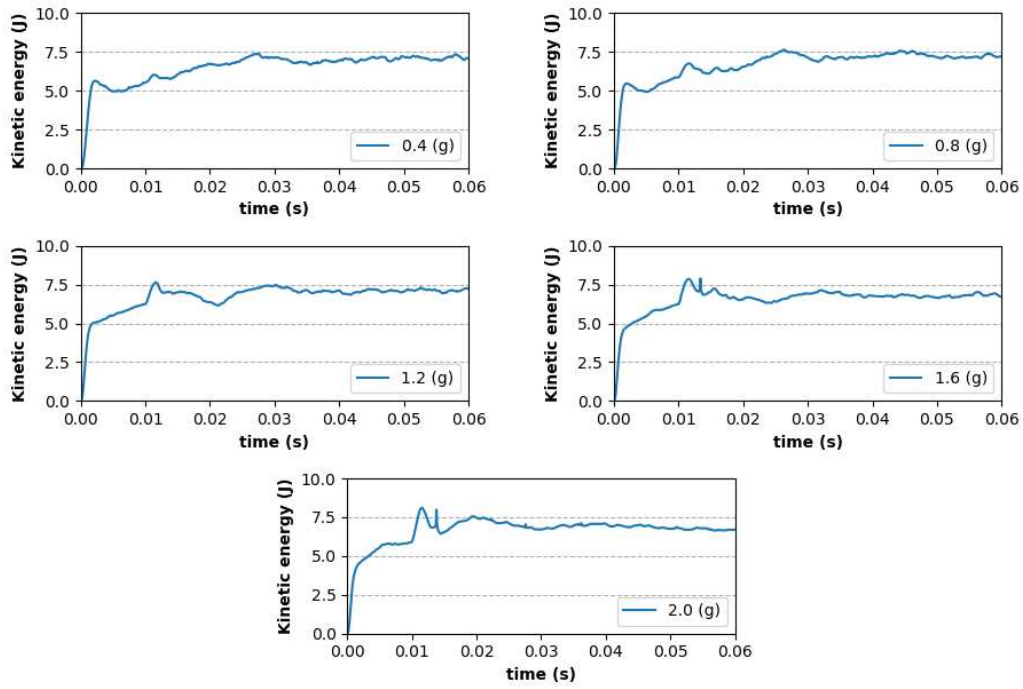
Figure 18: **Temporal variations of the total particle kinetic energy accumulated from time t = 0 s to 0.06 s**
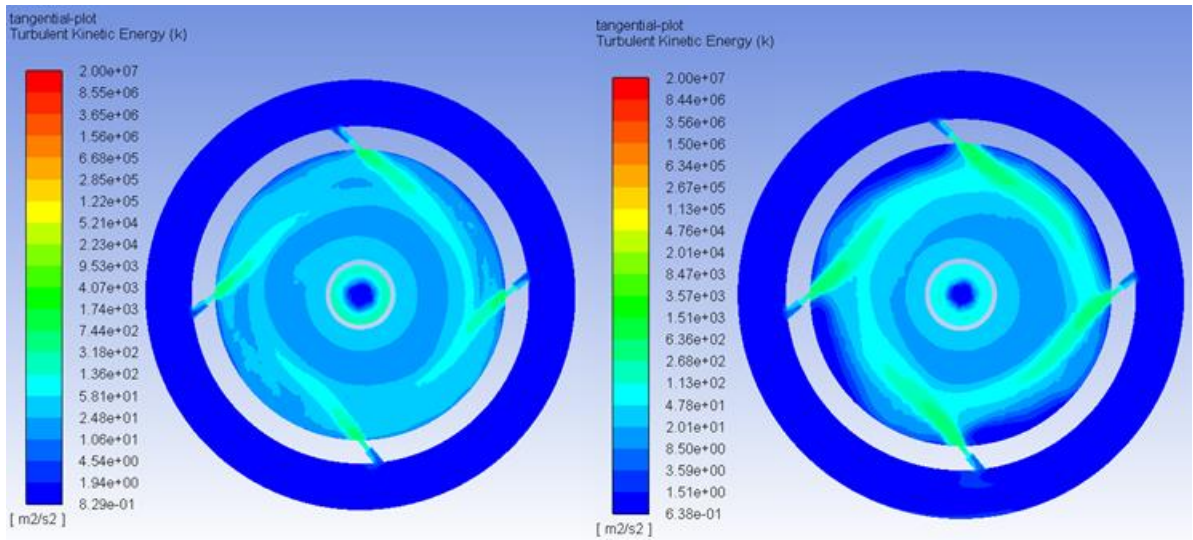

Figure 19: Turbulent kinetic energy (J/kg) plot of the fluid flow field for 0.4 g and 2.0 g holdup loadings after t = 0.06 s.
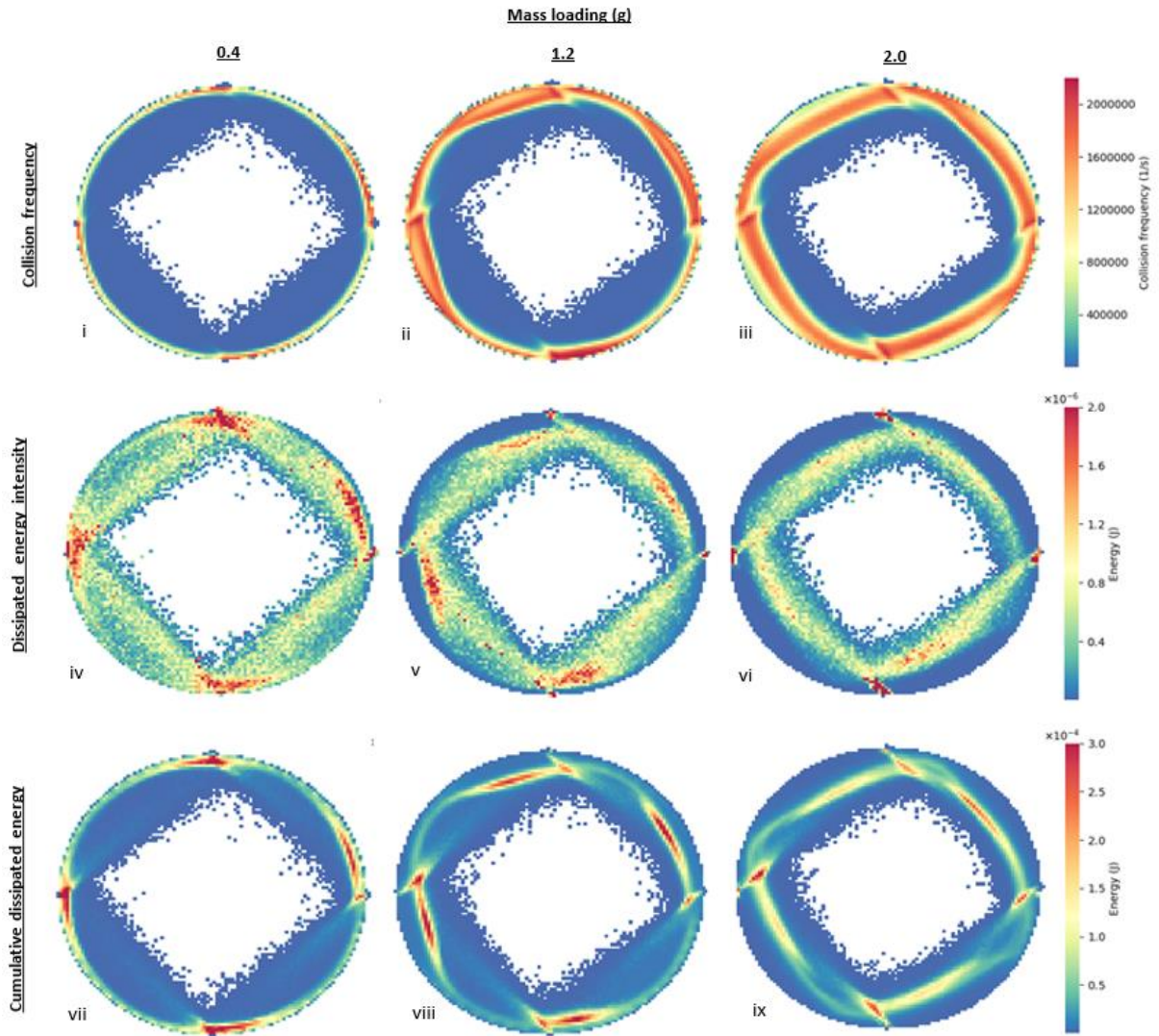
Figure 20: Contour plots depicting the spatial distribution of collision frequency and dissipated energy within the milling chamber for the 0.4 g, 1.2 g and 2.0 g loadings. The data are collected from t = 0.03 s till 0.06 s.

Table 3: Holdup mass loadings and particle size distribution used in the simulations

Mass loadings (g)		0.4, 0.8, 1.2, 1.6, 2.0
Particle diameter (μm) and size distribution (wt%)	300	20
	240	40
	200	20
	160	20
Number loading for each mass loading (g)	0.4	54321
	0.8	111005
	1.2	168013
	1.6	224206
	2.0	280366

Table 4: Fluid and particle properties and associated simulation conditions

Phase	Parameter	Value
Fluid	Viscosity, Pa/s	1.8×10^{-5}
	Grinding nozzle pressure, kPa	300
	Feed nozzle Pressure, kPa	320
	Fluid time step, s	$8 \times 10^{-6} - 2 \times 10^{-5}$
	Minimum cell edge length, μm	670
Particle	Density, kg/m^3	1500
	Shear modulus, MPa	10
	Poisson's ratio	0.25
	Coefficient of restitution	0.5
	Coefficient of static friction	0.5
	Coefficient of rolling friction	0.01
	DEM time step, s	$4 \times 10^{-7} - 1 \times 10^{-6}$